REPORT

Geology of the Caloris Basin, Mercury: A View from MESSENGER

Scott L. Murchie,[1] Thomas R. Watters,[2] Mark S. Robinson,[3] James W. Head,[4] Robert G. Strom,[5] Clark R. Chapman,[6] Sean C. Solomon,[7] William E. McClintock,[8] Louise M. Prockter,[1] Deborah L. Domingue,[1] David T. Blewett[1]

The Caloris basin, the youngest known large impact basin on Mercury, is revealed in MESSENGER images to be modified by volcanism and deformation in a manner distinct from that of lunar impact basins. The morphology and spatial distribution of basin materials themselves closely match lunar counterparts. Evidence for a volcanic origin of the basin's interior plains includes embayed craters on the basin floor and diffuse deposits surrounding rimless depressions interpreted to be of pyroclastic origin. Unlike lunar maria, the volcanic plains in Caloris are higher in albedo than surrounding basin materials and lack spectral evidence for ferrous iron-bearing silicates. Tectonic landforms, contractional wrinkle ridges and extensional troughs, have distributions and age relations different from their counterparts in and around lunar basins, indicating a different stress history.

The Caloris basin, the youngest large impact basin known on Mercury, was seen in its entirely during the first encounter of Mercury by the MESSENGER spacecraft in January 2008 (*1*). Caloris provides important information for understanding Mercury's geology because it exposes layering of the planet's crust, and it contains tectonic and volcanic features that are well-preserved as compared with those of older basins more modified by subsequent impact cratering. Imaging coverage of the basin interior and ejecta was therefore a focus of the encounter sequence. Here we make use of color and high-resolution monochrome images to reconstruct the geological evolution of the basin and to assess the origin and distribution of smooth plains material interior to the basin, the compositional stratification of Mercury's upper crust, and the large-scale deformational history of the region.

Over 30 years ago, Mariner 10 imaged the eastern part of Caloris (*2–5*), and the basin has subsequently been studied with ground-based radar (*6*). Major units forming the basin include a rim of concentric massifs with intermontane plains (the Caloris Montes and Nervo Formations), which form an annulus varying in width (up to 250 km) surrounding the light-colored basin in-

terior (Fig. 1A). An outlying darker annulus consists of rolling ejecta deposits (the Odin Formation), which grade into radially lineated plains and overlapping secondary craters in clusters, thought to be distal sculpted ejecta (the van Eyck Formation). These formations are comparable to counterparts in lunar basin materials, such as the Montes Rook and Hevelius Formations that surround the Orientale basin (*7*). Two types of smooth plains were recognized in association with Caloris. Exterior to the basin, annular smooth plains east of Caloris exhibit pervasive wrinkle ridges. The interior of the basin contains plains proposed on the basis of Mariner 10 images to have originated either as volcanic flows (*2, 8*) or impact melt (*9*). In the former case, the interior plains would be equivalent to lavas forming Mare Orientale, and in the latter to the Maunder Formation, which is thought to be impact melt. The interior plains exhibit wrinkle ridges and younger, cross-cutting extensional troughs (*10–12*). Wrinkle ridges, thought to have formed by a combination of thrust faulting and folding (*13–15*), occur near the eastern basin margin and are both concentric and radial to the basin, a pattern common in mare basalt-filled lunar basins. The troughs are graben formed by extensional stresses and have linear and sinuous segments that form giant polygons (*10, 11, 15*). Before MESSENGER, it was not known if or how far the wrinkle ridges and graben extended westward into the then-unimaged portion of the basin, or how consistent their spatial and age relations were across the basin.

Imaging by the Mercury Dual Imaging System (MDIS) (*16*) during MESSENGER's first Mercury flyby was optimized for coverage of Caloris, with a narrow-angle camera mosaic at 200 to 300 m/pixel, and a wide-angle camera 11-color mosaic at 2.4 km/pixel. Both data sets were

photometrically corrected to normalized reflectance at a standard geometry (30° incidence angle, 0° emission angle) and map-projected. From the 11-color data, principal component analysis and spectral ratios were used to highlight the most important trends in the data (*17*). The first principal component dominantly represents brightness variations, whereas the second principal component (PC2) isolates the dominant color variation: the slope of the spectral continuum. Several higher components isolate fresh craters; a simple color ratio combines these and highlights all fresh craters. PC2 and a 480-nm/1000-nm color ratio thus represent the major observed spectral variations (Fig. 1B).

The images show that basin exterior materials, including the Caloris Montes, Nervo, and von Eyck Formations, all share similar color properties, which continue with little variation azimuthally around the basin from the part imaged by Mariner 10 (Fig. 1). They have a normalized reflectance of ~0.085 at 560 nm, a red lunarlike spectral continuum, and an absence of light-colored smooth plains that occur as patches in the surrounding highlands (*17, 18*). Smooth plains within the Odin Formation lack distinctive color properties. In contrast, Caloris interior plains are about 10% higher in normalized reflectance and have a redder spectral continuum. The northwestern half of the interior plains is both slightly redder and slightly higher in albedo than the southeastern half. The interior plains exhibit craters with diameters of several tens of kilometers whose interiors and ejecta have a lower albedo and less red color than the basin exterior and resemble darker terrain exterior to the basin (red circles, Fig. 1A). The northwestern part of the basin interior exhibits craters with similar dark rims but light floors resembling the interior plains (blue circles, Fig. 1A). The margin of the basin contains diffuse, 30- to 100-km-diameter patches of very red material, typically ~40% higher in normalized reflectance than the basin exterior (red patches in Fig. 1B, circled in white). Fresh impact craters with comparably elevated albedo are spectrally distinctive from the red patches, with a less red spectral continuum than other materials (bluer color in Fig. 1B) as is also typical of fresh lunar craters (*19*).

Higher-resolution views of the western annulus (Fig. 1, C to E) show smooth to rolling plains surrounding the edge of the basin, which grade into radially lineated equivalents of the van Eyck Formation, particularly in the northwest (white arrow, Fig. 1C). The northwestern part of the basin interior also exhibits interior plains embaying knobs of the basin rim as well as a partly preserved inner ring, whose eastern portion was suggested in Mariner 10 images but not identified definitively (*2*) (red arrows, Fig. 1C). The western equivalent of the Caloris Montes Formation (red arrows, Fig. 1D) is an inward-facing scarp broken into clusters of knobs, locally higher in normalized

[1]Johns Hopkins University Applied Physics Laboratory, Laurel, MD 20723, USA. [2]Center for Earth and Planetary Studies, National Air and Space Museum, Smithsonian Institution, Washington, DC 20015, USA. [3]Department of Geological Sciences, Arizona State University, Tempe, AZ 85251, USA. [4]Department of Geological Sciences, Brown University, Providence, RI 02906, USA. [5]Lunar and Planetary Laboratory, University of Arizona, Tucson, AZ 85721, USA. [6]Southwest Research Institute, 1050 Walnut Street, Boulder, CO 80302, USA. [7]Department of Terrestrial Magnetism, Carnegie Institution of Washington, Washington, DC 20650, USA. [8]Laboratory for Atmospheric and Space Physics, University of Colorado, Boulder, CO 80303, USA.

Fig. 1. Overview of the Caloris basin. All images are mosaics in equirectangular projection, and north is up. (**A**) Enhanced (but still subtle) color image map showing 1000-, 750-, and 480-nm images in the red, green, and blue image planes. Yellow boxes are insets shown at higher resolution in (C), (D), and (E); red circles indicate superposed dark craters; blue circles indicate embayed dark craters; and the black arrow indicates the central crater Apollodorus of the radial graben complex. (**B**) Same view after data transformation. PC2, which captures variations between light plains and darker terrain, is shown in the green image plane and inverted in the red plane. The ratio of normalized reflectances at 480 nm/1000 nm, which highlights fresh impact ejecta, is shown in the blue plane. Small red spots are extremely red and elevated in albedo; those in white circles are centered on small rimless depressions. Thicker circles indicate features shown in Fig. 3. (**C**) High-resolution view of inset c in (A), showing radially lineated ejecta (white arrow) and massifs embayed by the interior plains (red arrows). (**D**) High-resolution view of inset d in (A), showing massifs at the inner edge of the western continuation of the Caloris Montes Formation (red arrows). (**E**) High-resolution view of inset e in (A), showing examples of wrinkle ridges (red arrows) and troughs (white arrows) in the southwestern interior plains.
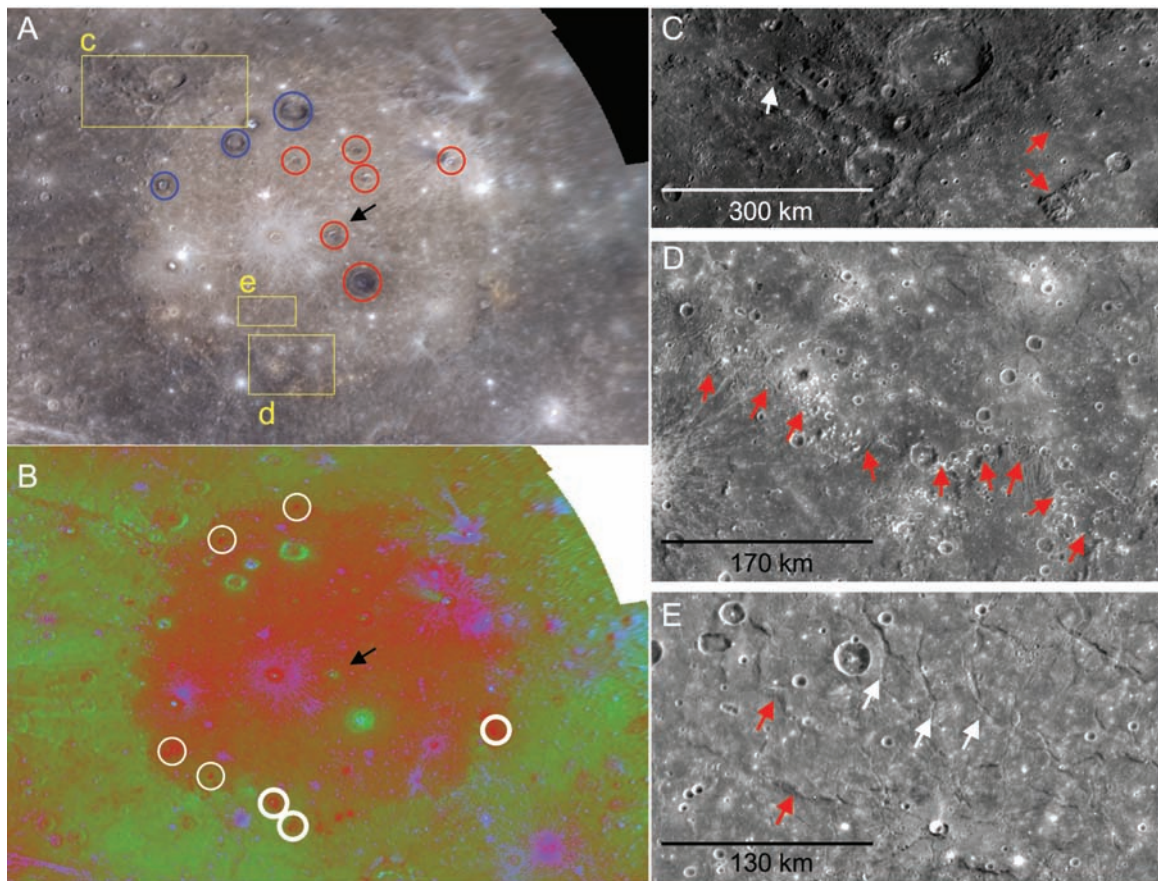
reflectance. Fitting the entirety of Caloris Montes yields a main basin ring diameter of 1550 km, as compared with 1340 km estimated from Mariner 10 data. The western interior plains (Fig. 1E) are deformed by both wrinkle ridges and extensional troughs, similarly to the eastern part of the plains imaged by Mariner 10. The continuity in color and morphology around the basin interior and exterior indicates that the units seen by Mariner 10 extend throughout the rest of the basin and its surroundings.

Two lines of evidence support the idea that the interior plains were emplaced by volcanism, as the stratigraphic equivalent of lunar maria rather than as Caloris impact melt deposits. The first line of evidence is the occurrence within the main basin ring of craters flooded by light-colored interior plains, analogous to lunar basin interior craters such as Archimedes in Mare Imbrium. Some interior craters (red circles, Fig. 1A) have color and morphology consistent with their superposition on the interior plains (left column, Fig. 2): unbroken crater rims and intact central peak rings; a gradual change in ejecta texture with radial distance from the crater rim;

and interior color and albedo properties consistent with the crater wall but distinct from surrounding plains, suggesting that an underlying dark layer was excavated. In contrast, craters interpreted as embayed and infilled (blue circles, Fig. 1A, and right column, Fig. 2) have attributes suggesting that they were flooded by interior plains material: breached rims and discontinuous central peak rings, an abrupt change in texture outside the crater where plains lap onto ejecta, and interior color properties distinct from the crater wall but matching the surrounding, lighter plains. Because the formation times of the several large craters on the Caloris floor must have spanned an interval much longer than that required for the emplacement of impact melts, the infilling of these craters must have occurred subsequently. Spudis and Guest (2) used Mariner 10 images and similar criteria to interpret a volcanic origin for light-colored interior plains of the Tolstoj basin, located to the southeast of Caloris. Interior flooding and embayment relations similar to these are also seen in smooth plains outside the Caloris basin in the MESSENGER data (17, 18).

The second line of evidence for volcanism is the presence of diffuse bright deposits concentrated along the margin of the basin (Fig. 3), associated with apparent volcanic structures (18). The bright deposits have a redder spectral continuum than other materials, in contrast to comparably bright fresh impact craters, which also typically display prominent rays (19). Moreover, the bright deposits are centered on irregularly shaped, scallop-rimmed depressions without raised rims. The morphology of these depressions does not resemble that of impact craters but is consistent with volcanic vents observed in the lunar maria (20). Similar diffuse deposits on the Moon are pyroclastic in origin (21), and we interpret these deposits to be pyroclastic as well. Spectrally similar materials are also observed surrounding somewhat degraded craters on the Caloris interior plains; these craters are smaller than those exposing dark material, suggesting that material resembling the diffuse deposits was excavated from a shallower depth in the interior plains.

Unlike the lunar maria, the Caloris interior plains are higher in albedo than the underlying basin material and lack spectral evidence for

Fig. 2. Examples of morphologic and spectral indicators of craters being superposed on the interior plains (Atget crater, left column) or embayed by interior plains material (unnamed crater, right column). The top row of images is from the narrow-angle camera high-resolution mosaic. The bottom row is transformed wide-angle camera color imagery, using the same representation of the data as in Fig. 1B. All images are mosaics in equirectangular projection, and north is up.
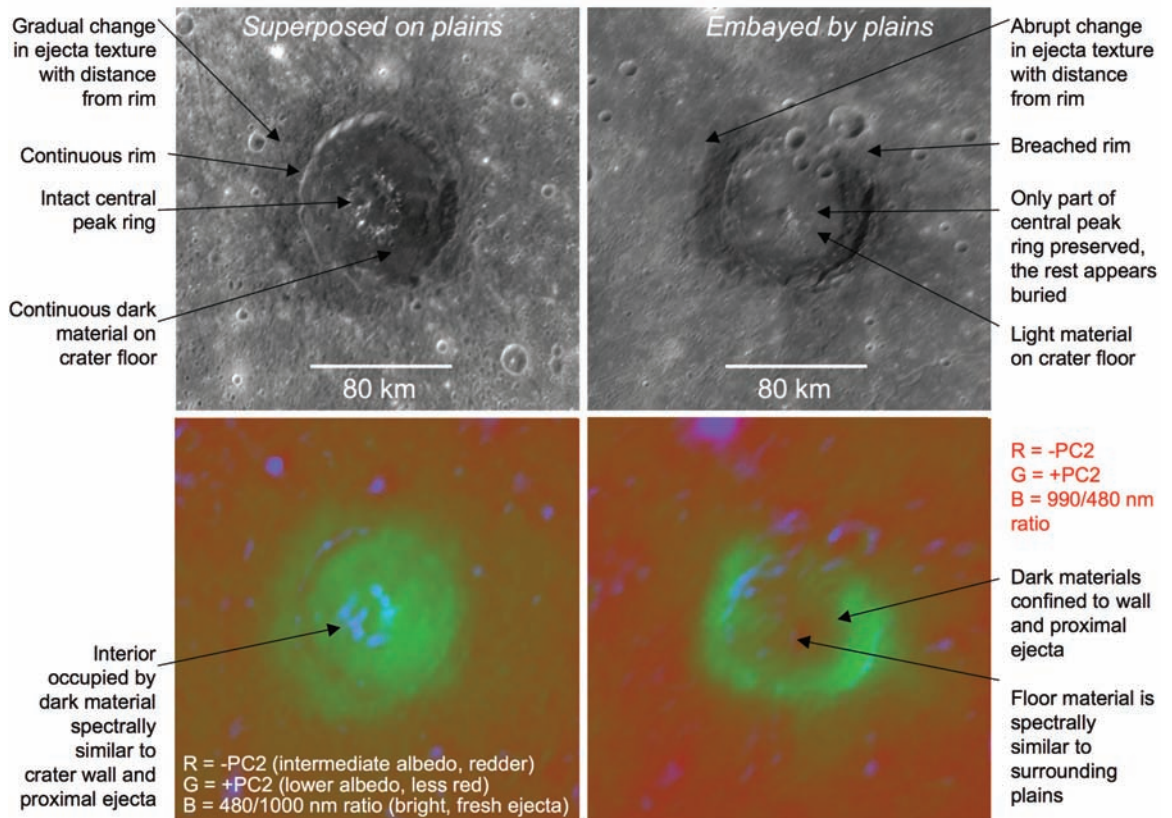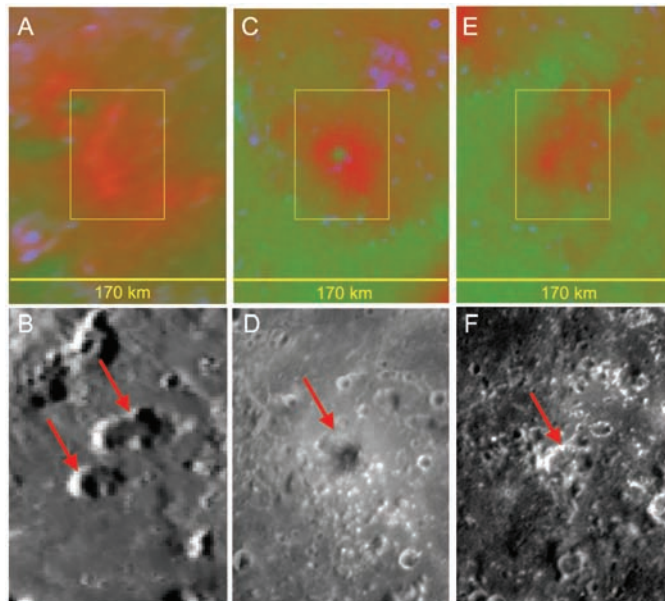

Superposed on plains — Gradual change in ejecta texture with distance from rim; Continuous rim; Intact central peak ring; Continuous dark material on crater floor; 80 km

Embayed by plains — Abrupt change in ejecta texture with distance from rim; Breached rim; Only part of central peak ring preserved, the rest appears buried; Light material on crater floor; 80 km

Interior occupied by dark material spectrally similar to crater wall and proximal ejecta

R = -PC2 (intermediate albedo, redder)
G = +PC2 (lower albedo, less red)
B = 480/1000 nm ratio (bright, fresh ejecta)

R = -PC2
G = +PC2
B = 990/480 nm ratio

Dark materials confined to wall and proximal ejecta

Floor material is spectrally similar to surrounding plains

Fig. 3. Spectral and morphologic characteristics of the diffuse red spots along the margin of Caloris, for the three spots with thick white outlines in Fig. 1B. The top row (**A**, **C**, and **E**) is transformed wide-angle camera color imagery, using the same representation of the data as in Fig. 1B. Each image in the bottom row (**B**, **D**, and **F**) is of the area shown in the yellow box in the image above. (D) and (F) are from the narrow-angle camera high-resolution mosaic, and (B) is from Mariner 10. Red arrows point to the central rimless, scalloped depressions. All images are mosaics in equirectangular projection, and north is up.

olivine, Mg- or Mg-Ca–rich pyroxene, or plagioclase feldspar.

MESSENGER images show that graben orientation progresses from a dominantly radial pattern at the center of the basin to a polygonal pattern at the edge of the basin. The outer graben overlap the radial distance range of wrinkle ridges (Fig. 4). The basin-radial graben include more than 230 linear troughs that converge near the center of the basin (~30°N, 163°E) as part of Pantheon Fossae, some of whose distal portions were previously mapped as part of the polygonal graben patterns in the Mariner 10 images of eastern Caloris (10, 11, 13). The measured lengths of individual graben range from ~5 to ~110 km, and widths range from less than 1 km up to a maximum of ~8 km. An impact crater about 40 km in diameter, Apollodorus, is located near the center of the complex (black arrow, Fig. 1, A and B). The crater's rim, wall, and floor expose dark material, as do other large craters superposed on the interior plains. The crater rim is not cross-cut by the graben, and proximal ejecta obscure the graben. These relations suggest that the graben postdate the plains and that the deposition of crater ejecta postdates the graben. Farther from the center of the basin, the polygonally arranged graben form a broad annulus of extensional deformation (Fig. 4). The distal graben of Pantheon Fossae appear as segments of the polygons and part of the regional extension. Wrinkle ridges extend farther from the basin center

silicates containing ferrous iron (Fe^{2+}). Neither fresh craters, nor the diffuse bright patches, nor any other materials exhibit a resolvable absorption at 0.90 to 1.05 μm (the 1-μm absorption) due to Fe-bearing olivine or pyroxene (17). Such an absorption feature is typical of young lunar craters superposed on either the lunar maria or average highlands. The lack of a 1-μm absorption suggests that the content of Fe in silicates is much lower than in the lunar maria (19); common igneous silicate minerals consistent with the absence of a 1-μm absorption include Mg-rich

Fig. 4. (**A**) Lambert conformal tectonic map of the Caloris basin showing graben (black) and wrinkle ridges (red), overlaid on a high-resolution narrow-angle camera mosaic. The map is based on available images with the most favorable illumination for recognizing morphology (MESSENGER narrow-angle images in the central part of the basin and Mariner 10 images in the eastern part of the basin). (**B**) High-resolution image of the inset of the Pantheon Fossae, indicated by the white box in (A). North is up.
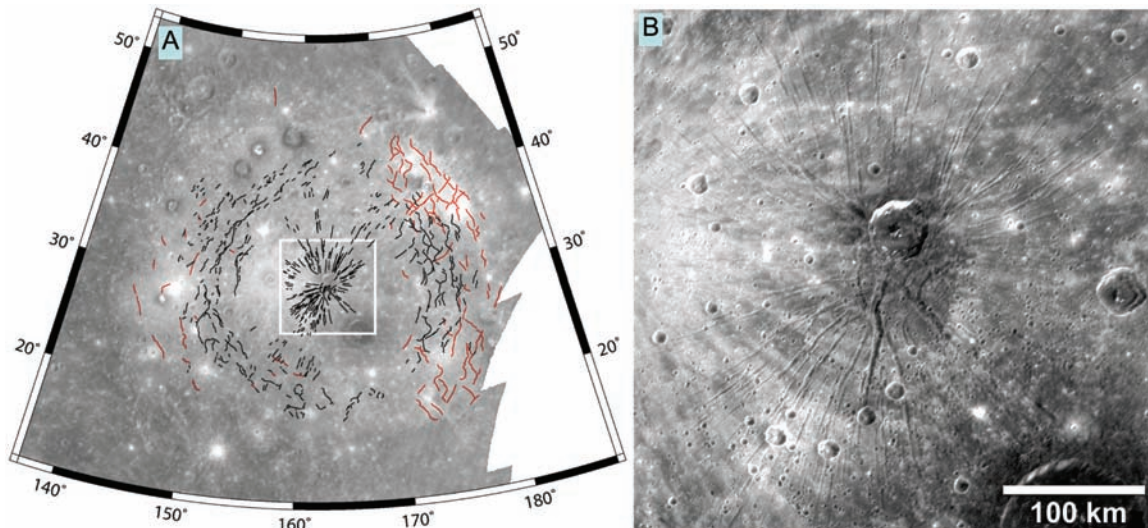
than do the graben. MESSENGER's high-Sun lighting geometry makes the recognition of low-relief ridges difficult; accordingly, a lower density of wrinkle ridges is recognized in MESSENGER imaging than in overlapping Mariner 10 imaging of eastern Caloris. The cross-cutting relations between wrinkle ridges and graben are consistent in both eastern and western Caloris; where the two types of features intersect, and their age relation can be determined, wrinkle ridges are always cut by and thus are older than the graben.

The pattern within Caloris of central radial graben and distal radial and concentric graben cross-cutting wrinkle ridges contrasts sharply with the spatial and temporal distribution of comparable features in lunar basins. In the lunar maria, wrinkle ridges occur predominantly in basin interiors, whereas graben are found in more distal parts or outside the basins (22, 23). Wrinkle ridges occur in the youngest lunar mare basalts, whereas lunar graben are restricted to the oldest basalts (24, 25). There is also no lunar counterpart to Pantheon Fossae. On the Moon, the distribution of wrinkle ridges and graben is thought to result from loading of the lithosphere by relatively dense, uncompensated mare basalt material, which induces subsidence and flexure of the lithosphere, leading to compression in the basin interiors and extension at the margins (23, 26). The spatial and temporal distribution of tectonic features in Caloris cannot be fully explained by such models. Wrinkle ridges in Caloris may have formed in response to subsidence of the interior plains (10), possibly aided by a compressional stress due to global contraction (11).

Two models have been proposed to account for interior extension in Caloris: exterior loading and lateral crustal flow. In the exterior loading model, the superposition of smooth plains exterior to the Caloris basin results in an annular load that causes basin-interior uplift and exten-

sion (10, 12). The lateral flow model involves movement of the lowest portions of postulated thick crust exterior to the basin inward toward the basin center, which causes late-stage uplift and extension (11). The central radial graben complex in Caloris presents a new constraint for these models, namely that tangential extensional stress exceeded radial extensional stress throughout the central basin region in order to account for the radial arrangement of the troughs. Another possibility is that Pantheon Fossae formed as the surface expressions of dikes that propagated radially from a magmatic intrusion near the basin center (18).

From the combination of MESSENGER and Mariner 10 data, six major phases in the history of the interior of the Caloris basin can be recognized: (i) formation of an impact basin and emplacement of impact melt (27) that must now be buried; (ii) superposition of several large craters in the basin interior; (iii) volcanic emplacement of light, redder material to form the interior plains, in part by pyroclastic and in part by effusive processes; (iv) formation (or continued activation) of wrinkle ridges in the outer part of the basin; (v) formation of radial and concentric graben; and (vi) superposition of still more impact craters, with smaller craters penetrating and excavating only the youngest volcanic plains and larger ones penetrating through to underlying darker material. Analysis of crater density variations (28) suggests that the emplacement of smooth plains exterior to the basin continued after phase (iii).

References and Notes

1. S. C. Solomon et al., Science **321**, 59 (2008).
2. P. D. Spudis, J. E. Guest, in Mercury, F. Vilas, C. R. Chapman, M. S. Matthews, Eds. (Univ. of Arizona Press, Tucson, AZ, 1988), pp. 118–164.
3. J. E. Guest, R. Greeley, U.S. Geological Survey (USGS) Miscellaneous Investigation Series, Map I-1408 (USGS, Denver, CO, 1983).
4. G. G. Schaber, J. F. McCauley, USGS, Map I-1199 (USGS, Denver, CO, 1980).
5. J. W. Head et al., Space Sci. Rev. **131**, 41 (2007).
6. J. K. Harmon et al., Icarus **187**, 374 (2007).
7. J. F. McCauley, Phys. Earth Planet. Inter. **15**, 220 (1977).
8. N. J. Trask, R. G. Strom, Icarus **28**, 559 (1976).
9. D. E. Wilhelms, Icarus **28**, 551 (1976).
10. H. J. Melosh, W. B. McKinnon, in Mercury, F. Vilas, C. R. Chapman, M. S. Matthews, Eds. (Univ. of Arizona Press, Tucson, AZ. 1988), pp. 374–400.
11. T. R. Watters, F. Nimmo, M. S. Robinson, Geology **33**, 669 (2005).
12. P. J. Kennedy, A. M. Freed, S. C. Solomon, J. Geophys. Res., in press, 10.1029/2007JE002992 (2008).
13. R. G. Strom, N. J. Trask, J. E. Guest, J. Geophys. Res. **80**, 2478 (1975).
14. T. R. Watters, J. Geophys. Res. **93**, 10236 (1988).
15. T. R. Watters, Icarus **171**, 284 (2004).
16. S. E. Hawkins III et al., Space Sci. Rev. **131**, 247 (2007).
17. M. S. Robinson et al., Science **321**, 66 (2008).
18. J. W. Head et al., Science **321**, 69 (2008).
19. C. M. Pieters, in Remote Geochemical Analysis: Elemental and Mineralogical Composition, C. Pieters, P. Englert, Eds. (Cambridge Univ. Press, New York, 1993), pp. 309–339.
20. J. W. Head, A. Gifford, Moon Planets **22**, 235 (1980).
21. J. B. Adams, C. Pieters, T. B. McCord, Proc. Lunar Sci. Conf. **5**, 171 (1974).
22. M. P. Golombek, J. Geophys. Res. **84**, 4657 (1979).
23. S. C. Solomon, J. W. Head, Rev. Geophys. Space Phys. **18**, 107 (1980).
24. B. K. Lucchitta, J. A. Watkins, Proc. Lunar Planet. Sci. Conf. **9**, 3459 (1978).
25. J. M. Boyce, Proc. Lunar Science Conf. **7**, 2717 (1976).
26. H. J. Melosh, Proc. Lunar Planet. Sci. Conf. **9**, 3513 (1978).
27. M. J. Cintala, J. Geophys. Res. **97**, 947 (1992).
28. R. G. Strom et al., Science **321**, 79 (2008).
29. N. Laslo, H. Kang, R. Vaughan, A. Harch, R. Shelton, and A. Berman designed the imaging sequences that made this contribution possible. B. Denevi, K. Becker, and C. Hash are gratefully acknowledged for data calibration and processing. The MESSENGER project is supported by the NASA Discovery Program under contracts NAS5-97271 to the Johns Hopkins University Applied Physics Laboratory and NASW-00002 to the Carnegie Institution of Washington.